Simulation of Convective Heat Loss through Mineral Wool in a Rainscreen Facade

M. Steven Doggett, Ph.D. and Robert F. Brunjes, AIA

Built Environments, Inc., Stillwater, Minnesota, U.S.A.

Abstract – This study applied Computational Fluid Dynamics (CFD) to determine the effects of wind-induced convection through mineral wool in a ventilated rainscreen system. Wind studies of a conceptual low-rise building subject to a wind speed of 6.7 m/s demonstrated dynamic airflows and rainscreen velocities ranging from 0.1 to over 3 m/s. Localized pressure fields near cladding support framing increased air velocities within the mineral wool by one to two orders of magnitude. These high pressure regions, together with increased surface flows at corner domains, represented the primary pathways governing convective heat loss. Simulated convection through mineral wool slabs showed that even high density materials are prone to increased heat transfer due to air permeability into the open pore volume. Vertical and horizontal flow regimes at 1 to 2 m/s increased heat transfer by 4 to 42% over the range of simulated mineral wool densities. Gaps between and behind insulation slabs further increased the convective effects, resulting in heat flux densities that were up to 62% higher than non-gapped, impermeable insulation. The results of this study support growing recognition that exterior mineral wool must be protected from the detriments of convective forces. Alternatively, adjustments in effective R-values should be made when using un-faced mineral wool slabs.

1. INTRODUCTION

The use of air-permeable fibrous insulation poses unique challenges for high-performing building enclosures that seek to combine the benefits of continuous exterior insulation with the improved moisture transport of ventilated rainscreens. Air permeability of un-faced materials, including higher density rock wool and glass wool products, exceed minimum requirements for effective air barriers. Current practices therefore place the air barrier interior of the exterior insulation owing to the logistics of installing effective air barriers over mineral wool panels that are often penetrated by cladding support systems. This approach inherently assumes that some measure of air is transferred beyond the insulation panel either through the insulation itself or at joints between insulation slabs and other enclosure components. The ramifications of these thermal bypasses depend on several factors, most notably the convective forces within the rainscreen cavity, air permeability of the insulation, and continuity of the insulation layer.

Airflow within rainscreen cavities results from driving forces collectively referred to as convection. Natural convection entails air movement originating from temperature gradients as forces are generated in the vertical direction in response to gravity and air density. In contrast, forced convection refers to air movement resulting from wind or mechanically-induced pressure gradients across and within the rainscreen cavity. Forced convection includes the commonly referenced term 'wind washing' where air moves across the surface of the insulation or, in the case where air actually penetrates the insulation, through the open pore volume. Unlike the vertical transport of density-dependent airflows, forced convection can generate highly turbulent, multi-directional flows as a function of venting characteristics, rainscreen

geometries, and increasing wind speed (Odewole and Edwards, 2011).

It is well recognized that wind-driven forces within rainscreens vary greatly and are influenced by factors such as building exposure, cladding type, rainscreen type, wind speed and direction, configurations of vent openings, solar radiation, cavity dimensions, and eave construction (Salonnvarra et al, 2007; Finch and Straube, 2007, Falk and Sandin 2013; Straube et al., 2004; Stovall and Karagiozis, 2004). It deserves noting that much of this knowledgebase reflects relatively simple rainscreen geometries consisting of a cladding system, a vented or ventilated air cavity, and backup wall with an air and water barrier (Figs. 1a, 1b). These systems have traditionally lacked exterior insulation. The flow-creating planes also tended to be simpler and semi-compartmentalized, resulting in more uniform, parallel flow paths. Modern rainscreens that integrate ventilation with exterior insulation often rely on complex cladding support systems such as girts, hat channels, and brackets (Fig. 1c). These attachment systems extend the full depth of the rainscreen cavity and are therefore more likely to disrupt the primary flow direction while also generating multi-directional turbulent mixing and localized high-pressure gradients.

Such dynamic rainscreen airflows are particularly relevant for mineral wool products as permeability through the open pore volume is known to play an important role in convective heat loss (Stankevičius et al., 2013). Air permeability of mineral wool is inversely proportional to bulk density, but additional properties such as fiber size, matrix composition, fiber orientation, and fiber inhomogeneity also influence the movement of air through the open pore volume (Lecompte, 1990; Hopkins, 2007; Schimidt and Kornadt, 2012).

Air permeability is also a function of the applied air pressure. For the purpose of standardization, the mineral wool industry derives permeability values from methods intended for acoustic testing; which, in accordance with ISO 9053/EN 29053, employs a pressure differential of only 0.2 Pa. The applicability of such low pressure differences has been questioned by Schmidt and Kornadt (2012).

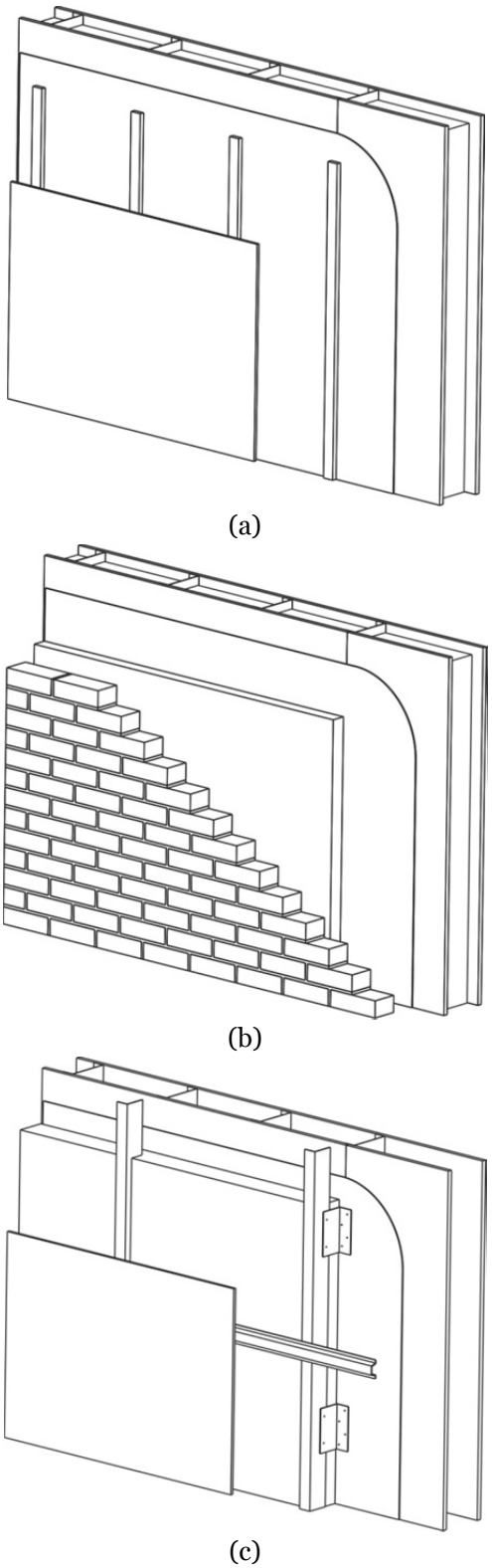

Fig. 1. Conceptual rainscreen systems.

Their findings showed that permeability of rock wool slabs was more than 30% higher when measured at realistic rainscreen pressure differences of 5 to 10 Pa as compared to earlier findings that utilized the 0.2 Pa standard.

There is sparse information available regarding the effects of forced convection through mineral wool. Laboratory studies commissioned by Roxul, Inc., found that simulated wind-washing at 1 m/s against slabs of various thicknesses (density = 70 kg/m^3) reduced thermal resistance by 1.5 to 9.5% (Stratten and Trainor, 2013). In comparison, research by Kosinski (2014) found that thermal resistance of loose mineral wool (density = 90 to 118 kg/m^3) was reduced by approximately 80 to 90% when exposed to wind speeds of 0.46 to 3.24 m/s. Stankevičius et al (2013) studied convective heat transfer through ventilated gapped walls insulated with rock wool with densities ranging from 22.3 to 57.6 kg/m^3. Their results showed that natural convection through unprotected insulation slabs increased heat transfer by 5 to 15%; whereas, under forced convection at 3 Pa, heat transfer increased by 7 to 25%. The risks of convective heat loss are even more pronounced when considering the effects of air gaps between unsealed friction-fitted slabs. For example, Hens et al. (2001) found that U-factors increased by 68% in unventilated walls configured with 1 cm air gaps between high density mineral fiber. The authors attributed their findings to both buoyancy flow as well as wind washing. Other studies have shown that gap dimensions, location, and distance of gap offsets at opposite sides of the wall significantly influence convective heat transfer (Svoboda, 1999; Stankevičius et al., 2013; Huttunen and Vinha, 2013; Kosinski, 2015). Gapping behind insulation slabs, especially when such voids are continuous with edge gaps, are particularly detrimental. Air voids between insulation slabs and the warm side of ventilated cavity may increase heat transfer by several orders of magnitude (Stankevičius et al., 2013).

The aim of this present study is to assess wind-induced airflows and its effects on convective heat transfer through mineral wool within a ventilated rainscreen system. Computational Fluid Dynamics are used to evaluate exterior building pressures, flow paths, and rainscreen air velocities for coupled, whole-building simulations. Heat transfer studies involving an uncoupled wall assembly further explore the effects of forced convection under winter design conditions. The effects of gapping between and behind the insulation slabs are also described.

2. METHODS

2.1 Numerical simulation

Simulations were performed with Autodesk Simulation CFD 2016. This computational software utilizes mathematical models and finite element analysis to predict simultaneous flows of fluids and heat in three-dimensional tetrahedral meshes. The CFD simulations conducted in this study were performed in accordance with the Autodesk application manual (Autodesk, 2016) and best practice guidelines (Casey and Wintergerste, 2000).

Preliminary sensitivity analyses evaluated several turbulence models, including k-epsilon, SST k-omega, RNG, and mixing length. The standard k-epsilon model was selected for final study based on early benchmarking with exterior building pressures, rainscreen airflows, and volumetric airflows through distributed resistance materials. This study also utilized the modified Petrov-Galerkin advection scheme as recommended by Autodesk Simulation CFD for improved stability in simulations involving natural and forced convection, distributed resistances, and conjugate heat transfer. The model's advection scheme defines the transport mechanism of heat flow as a result of the bulk motion of air through an air-permeable matrix.

Numerical simulations were performed in three-phases. The first phase involved a steady-state wind study in which exterior airflows were introduced to a conceptual low-rise building configured with a back-ventilated rainscreen.

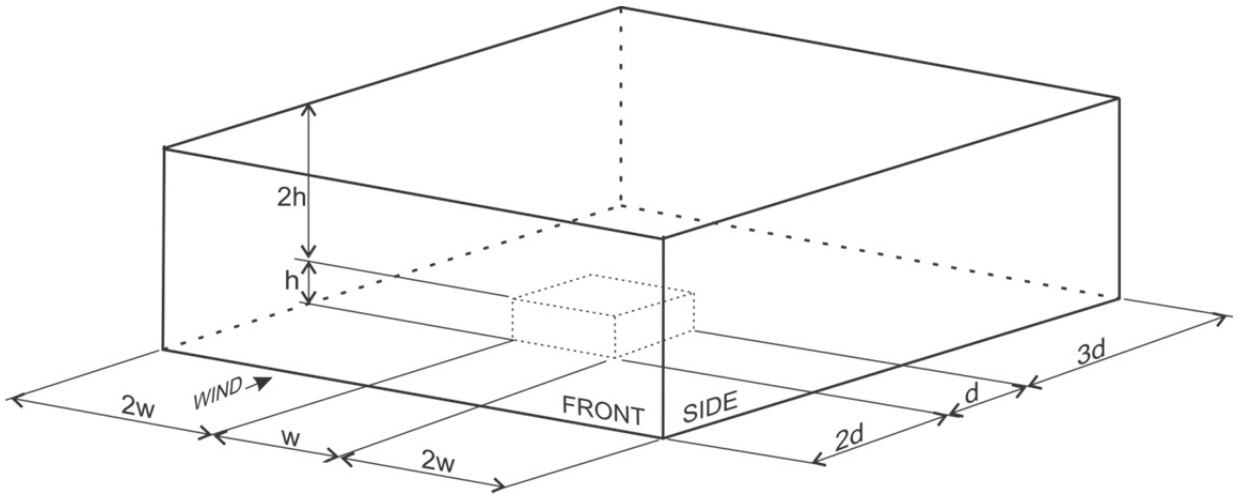

Fig. 2. Dimension ratios of building and exterior air domain.

Wind pressures, velocities, and general airflow patterns for exterior surfaces of the building and rainscreen cavities were assessed simultaneously. For the second phase, convective heat transfer was simulated by transferring boundary conditions derived from the wind study to a smaller representative wall. This uncoupled approach enabled improved solution accuracy of conjugate heat transfer through the rainscreen cavity and exterior insulation. The same approach was utilized for the third phase of the study where convective heat loss was assessed in response to air gaps between mineral wool slabs. For all phases of this study, the effects of solar radiation and air buoyancy were not assessed.

2.2 Wind study

Whole building wind studies were performed on a conceptual low-rise building with opaque walls. Building dimensions were fixed at 12.5 m x 12.5 m x 4.0 m (w x l x h) and placed within the exterior air volume as shown in Fig. 2. The specific ratios of dimensions for the exterior domain reflect best practices as recommended by Autodesk Simulation CFD for exterior wind studies (Autodesk, 2016).

Solid modeling of the concept building included a wall assembly with highly detailed components as shown in Figs. 3a-3c. The wall represents 152 mm (6 in) steel stud construction at 406.4 mm (16 in) on center spacing. The cladding support system consisted of vertical L-girts with brackets and hat channels. The vertical girts were centered every 812.8 mm (32 in) and attached to 152 mm (6 in) long L-brackets installed 665 mm (26.2 in) on center vertically. Horizontal hat channels 22 mm (0.875 in) deep x 63.5 mm (2.5 in) high were attached to the vertical girts at 1,201 mm (47 in) intervals vertically. A single layer of mineral wool 102 mm (4 in) thick was assumed to be friction fitted between the vertical girts and behind the hat channels. A continuous air space between the backside of the hat channels and the mineral wool was 25.4 mm (1 in). This provides a combined airspace of 47.6 mm (1.8 in) between the cladding and mineral wool. A continuous clear vent space of 25.4 mm (1 in) was provided at the top of the wall between the cladding and roof coping.

The interior wall cavity lacked insulation and was sheathed on both sides by 15.9 mm (0.625 in) thick gypsum board panels. The nominal R-value of the assembly without wall framing and exterior cladding support system was determined to be 20.7 (ft^2F h/Btu), and the effective R-value with framing and cladding support system was 15.1.

The thin-layered weather-resistive barrier was not modeled in this study as Autodesk Simulation CFD considers solid materials to be impermeable to air. Likewise, to minimize computation times, framing fasteners and attachment pinning of the mineral wool were not modeled.

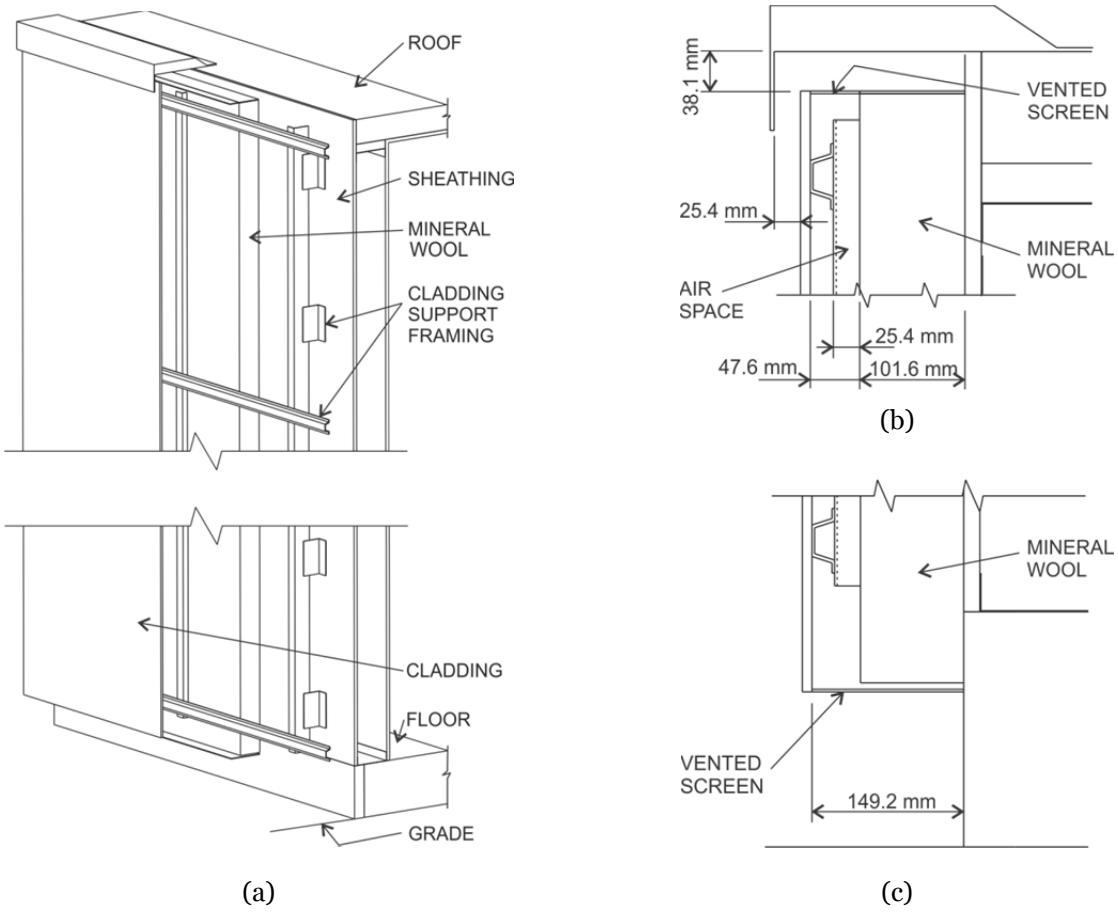

Fig. 3. Whole-building wall assembly (a) with detail sections of top (b) and bottom (c).

The rainscreen was representative of modern back-ventilated systems where the rainscreen cavity depth and geometries are largely dictated by the cladding support framing. Continuous vent screens were placed at the top and bottom of all four walls. The upper vent screen consisted of two-parts where the portion directly above the insulation was modeled as a solid to prevent airflow through the mineral wool insulation at the interface with the upper vent. The remaining portion of the vent screen was simulated as a distributed resistance with a free area ratio of 0.43, which corresponds to a screen with 3.18 mm (0.125 in) perforations. This approach reduces the meshing requirements that are otherwise necessary when modeling volumes with complex vented geometries (Autodesk, 2016). The bottom screen was fully vented with a free area ratio of 0.43 for the entire rainscreen depth. The aforementioned screen configurations were based on preliminary findings showing that the upper vent screen served as the primary inlet. Resulting flows at the windward wall were vertical and top-down. Selection of mineral wool slabs for rainscreen applications is often determined by the expected ventilation intensity as determined by the ventilation opening area (Endriukaitytė et al., 2009; Paroc, 2016). In this case, the ventilation opening area was approximately 189 cm^2/m without the perforated screen or 76 cm^2/m with the perforated screen. This configuration would be classified as 'ventilated' according to the aforementioned schemes.

To simulate wind within the exterior domain, boundary conditions included an inlet velocity of 6.7 m/s (15 mph) and an outlet of 0 Pa relative pressure at the leeward exterior boundary. The

top and two sides of the exterior boundary were defined by slip symmetry, which enables the fluid air to flow along the boundary wall rather than against it. The exterior air volume was free to interface with a separate, more tightly meshed rainscreen air volume by means of the top and bottom vent screens. This study employed the simulation software's default variable air settings for the exterior and rainscreen air volumes. A roughness factor of 4.7 mm was applied to the rainscreen cavity air. The CFD solver automatically applies this value to the adjacent mineral wool. All remaining rainscreen surfaces were simulated as a smooth zero-roughness wall.

2.3 Heat transfer study

Wind-induced heat transfer was assessed using a simplified wall assembly having the same construction as the rainscreen wall used in the wind loading study (Fig. 4). Vent screens were removed and the wall was reduced to fixed dimensions of 2.3 m x 2.5 m (*w x l*). This assembly-based approach was necessary to achieve the meshing refinement necessary for accurate, simultaneous solutions of air and heat transfer through air-permeable materials. Material properties of the wall components are listed in Table 1.

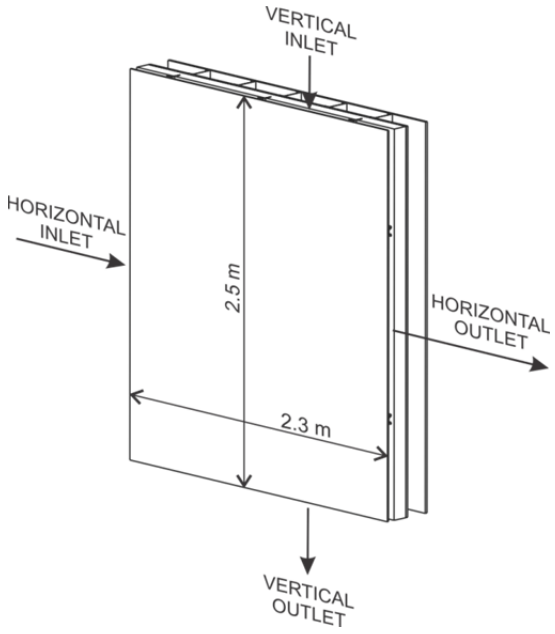

Fig. 4. Heat transfer wall with flow regimes.

Table 1. Material properties of wall components.

	d (mm)	ρ (kg/m³)	λ (W/m-K)	c (J/kg-K)
Fiber Cement	9.53	1,675	0.40	840
Rainscreen Air	47.6	*	0.026	1,004
Vertical Girts	2.54	7,833	55	465
Steel Brackets	2.54	7,833	55	465
Mineral Wool	101.6	30 - 160	0.032	850
Gypsum Sheathing	15.9	800	0.17	840
Steel Studs	1.09	7,833	55.0	465
Wall Cavity	152.4	1.3	0.940	1,000
Gypsum Wallboard	15.9	800	0.17	840

d = thickness; ρ = density; λ = conductivity; c = heat capacity
* density of air is modeled by Autodesk Simulation CFD as equation of state

Two flow regimes were established to represent general airflow patterns demonstrated by the wind study findings (Fig. 4). Separate vertical and horizontal flow regimes were established with inlet air velocities of 1 m/s and 2 m/s placed at the top (vertical flow) or side (horizontal flow) of the rainscreen air boundary. Inlet velocities were representative of airflow characteristics that occurred downstream of the vent screens as demonstrated by the whole-building wind study.

Air outlets were simulated with 0 Pa relative pressure applied at the opposite air boundary condition. Slip symmetry conditions were assigned to remaining surfaces.

Simulations assumed interior and exterior ambient temperatures of 21°C and -5°C, respectively. These design parameters represent winter conditions that occur over a large segment of North America. A heat transfer film coefficient of 8.3 W/m²/K was

applied as boundary conditions at the interior gypsum board and exterior fiber cement siding.

Air permeability values selected for this study reflect the known linear relationship between mineral wool density and air resistivity as summarized by Hopkins (2007). Review of product offerings by mineral wool manufacturers indicate that un-faced slabs intended for rainscreen applications range from 33 kg/m^3 to 200 kg/m^3.

Permeability as referenced in this study is symbolized as k, or intrinsic permeability, and expressed as length squared based on Darcy's Law:

$$Q = \frac{Ak\Delta P}{\mu \Delta x} \qquad (1)$$

where: Q is the volumetric fluid flow rate through the medium; A is the area of the medium; k is the permeability of the medium; μ is the dynamic viscosity of the fluid; ΔP is the applied pressure difference; and Δx is the thickness of the medium. For the purpose of clarity, these k-values are listed in Table 2 with the correponding bulk densities as well as the flow coefficients for permeability and resisitivity. Resisitivity values reflect an assumed air viscosity cefficient of 1.8 x 10^{-5} at 20°C. Permeability is the reciprocal of resisitvity.

Table 2. Air permeability, resistivity, and estimated density of simulated mineral wool.

Permeability (m^2)	Permeability (m^3/Pa·m·s)	Resistivity (Pa·s/m^2)	Density (kg/m^3)
2.0 x 10^{-10}	11.1 x 10^{-6}	90,000	160
4.0 x 10^{-10}	22.2 x 10^{-6}	45,000	90
6.0 x 10^{-10}	33.3 x 10^{-6}	30,000	80
8.0 x 10^{-10}	44.4 x 10^{-6}	22,500	70
1.0 x 10^{-9}	55.5 x 10^{-6}	18,000	50
1.5 x 10^{-9}	83.3 x 10^{-6}	12,000	40
2.0 x 10^{-9}	111 x 10^{-6}	9,000	30

2.4 Insulation gap study

The effects of insulation gaps on convective heat transfer were assessed by introducing gaps to the heat transfer wall. A single permeability value 1.0 x 10^{-9} m^2 was selected to represent a medium density slab (50 kg/m^3) currently marketed for rainscreen applications.

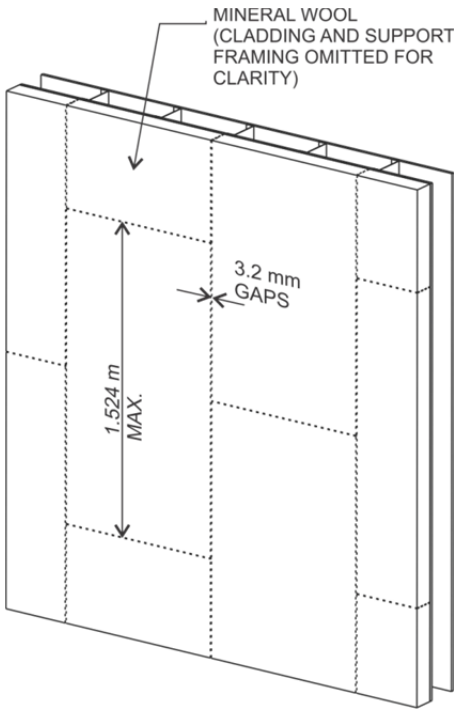

Fig. 5. Location of edge gaps.

Slab edge gaps with widths of 3.2 mm were modeled as fluid air and as an extension of the rainscreen cavity volume. The placement and orientation of these gaps are shown in Fig. 5. Edge gaps located adjacent to vertical girts extended the full wall height (2.5 m) in the vertical direction and from girt to girt (0.8 m) in the horizontal direction. The total air volume introduced by the gaps was 0.004 m^3. Additional gapping in the form of a single contiguous air film (0.8 mm) was introduced behind the mineral wool slab. The aim of this approach was to simulate gaps that occur when the mineral wool is poorly pinned or un-adhered to the face of the sheathing. The additional air volume created by the interstitial gap was 0.004 m^3, for a total air gap volume of 0.008 m^3 and a total rainscreen volume of 0.279 m^3.

Boundary conditions used in the baseline heat transfer study were also employed here for the assessment of air gaps.

2.5 Validation

The CFD models were compared to published research, sparsely available manufacturer data, and additional validated software for the purpose of benchmarking and validation. The basis for comparisons included exterior building pressure, rainscreen pressure differentials, rainscreen flow velocities, and airflow rates through the rainscreen mineral wool. Where relevant, these comparisons are discussed with the corresponding results. Benchmarking for heat transfer and air permeability was particularly relevant for this study; therefore, these procedures are discussed here in further detail.

Accurate simulation demanded resolution of four primary processes: 1) conduction; 2) forced convection through the rainscreen cavity; 3) air permeability through the mineral wool; and 4) natural convection within the isolated air-filled wall cavity. The first two processes were addressed through refined uniform meshing combined with the application of a robust advection scheme. The third process was also addressed by refined meshing in conjunction with the permeability function of Autodesk Simulation CFD as described further below and by Eq. 2. For the fourth process, thermal conductivity of air within the isolated wall cavity required solving for natural convection. Meshing requirements for this free convection issue limited the computational resources necessary for solving convection and permeability problems on the rainscreen side of the wall. Because the air-filled wall cavity did not influence the exterior convective forces, the air volume was modeled as a solid with the material properties of fluid air. This was performed using the thermal conductivity of 0.94 W/mK for a 150 mm air volume as provided by the material database of WUFI® version 5.3. Heat transfer studies of walls that lacked framing were performed with Autodesk Simulation CFD and WUFI®. These comparisons yielded temperature gradients that varied by less than 0.5°C at all corresponding points through the full wall depth. This agreement was considered to be robust, especially in light of the dimensional disparity between the 150 mm WUFI air volume and the 152.4 depth of the modeled air volume.

The air permeability of mineral wool was simulated with the permeability function in Autodesk Simulation CFD. This function is designed to represent fluid movement through porous media based on Darcy's Law (Eq. 1). The permeability function used by Autodesk Simulation CFD provides a constant resistance in all directions. Pressure drop as a function of permeability is expressed as:

$$\frac{\partial p}{\partial x} = C\mu u_i \qquad (2)$$

where C is the viscosity coefficient, μ is the viscosity (of the surrounding fluid) and u_i is the velocity in the global i coordinate direction.

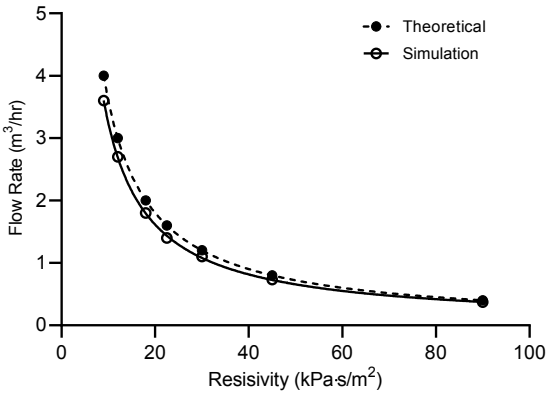

Fig. 6. Theoretical and simulated flow rates.

The permeability function of Autodesk Simulation CFD was benchmarked by determining flow rates through 1 m3 of mineral wool at a pressure differential of 10 Pa. Utilizing Darcy's equation and an assumed air viscosity of 1.8 x 10^{-5}, the theoretical flow rates were compared to the simulated results as a function of air resistivity. Good agreement and a variation of approximately 0.8 to 2% were achieved from the highest to lowest resistivity (Fig. 6).

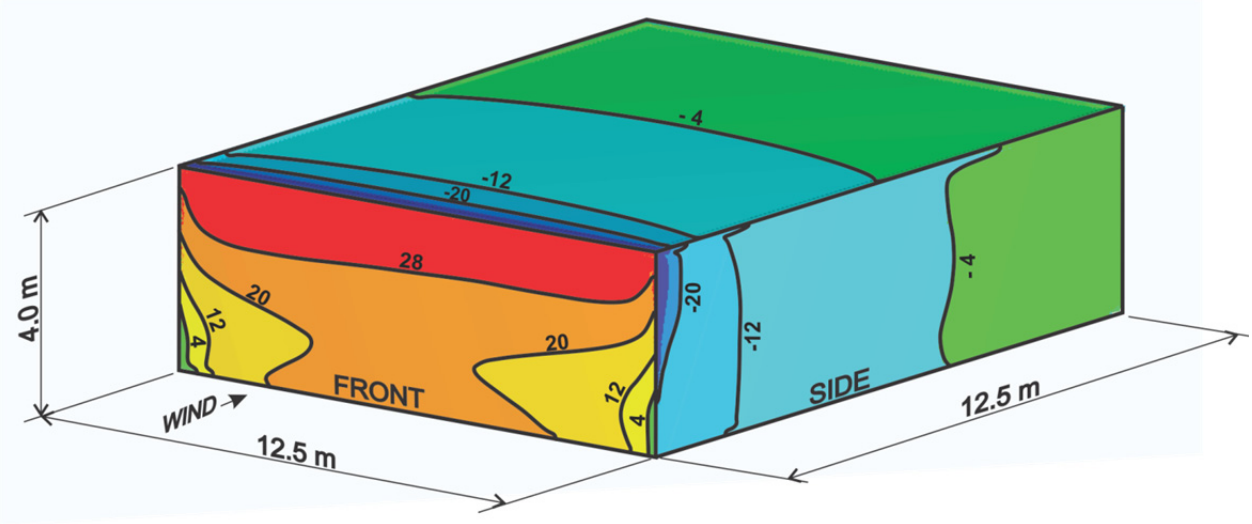

Fig. 7. Exterior building pressures (Pa).

3. RESULTS AND DISCUSSION

3.1 Exterior building pressures

Static air pressures resulting from a steady-state wind velocity of 6.7 m/s (15 mph) are summarized by Fig. 7. Despite the relatively small size of the building, the simulation results were able to resolve patterns that conform to known principles of wind loading for low-rise buildings (ASHRAE, 2009 and ASCE, 2010). The pressure fields for windward surfaces generally ranged from 4 to 35 Pa with the greatest pressures exerted at the center and upper portions of the building. Side elevations exhibited negative pressure gradients ranging from -50 Pa near the front of the building to approximately -4 Pa near the leeward corners. A small negative pressure gradient of -3 Pa to -5 Pa was predicted for leeward surfaces.

3.2 Rainscreen airflows

Rainscreen airflow and velocities shown in Figs. 8a-8c represent section views obtained at approximately 12 mm from the insulation face. The primary direction of inlet flow depended on exterior building pressures and the established wind-induced pressure fields within the rainscreen. At the windward wall, air flowed primarily from top to bottom with the bottom vent serving as the primary outlet. Flow was predominately vertical at the center of the building, transitioning from diagonal to horizontal in approach of the negative pressure region at the windward corners. Air velocities for the windward wall ranged between 0.7 to 1.3 m/s throughout most of the referenced section plane. Significantly higher velocities were predicted for regions near cladding support framing and corner domains. For example, air velocities behind the upper hat channels exceeded 2.5 m/s for the full width of the wall. These localized velocity fields were repeated behind each hat channel until diminishing near approach to the bottom vent opening. Similarly, airflows over the vertical girts increased as airflows approached the corner domains. Examples of increased velocity fields in association with the cladding support system are shown in Figs. 9a and 9b. In general, the cladding support framing disrupted the vertical and horizontal planes creating localized areas where airflows and velocities varied remarkably from the main fields.

Rainscreen airflows within the side walls exhibited very different characteristics. Air moved horizontally from windward and leeward corners and released at the upper and lower vents (Fig. 8b). As expected, air velocities within the side walls were significantly lower than those predicted for the windward rainscreen. Air speeds ranging from 0.2 to 0.6 m/s were typical. Higher velocity fields were predicted for the windward corner domains where air speeds ranged from 0.8 to 3 m/s.

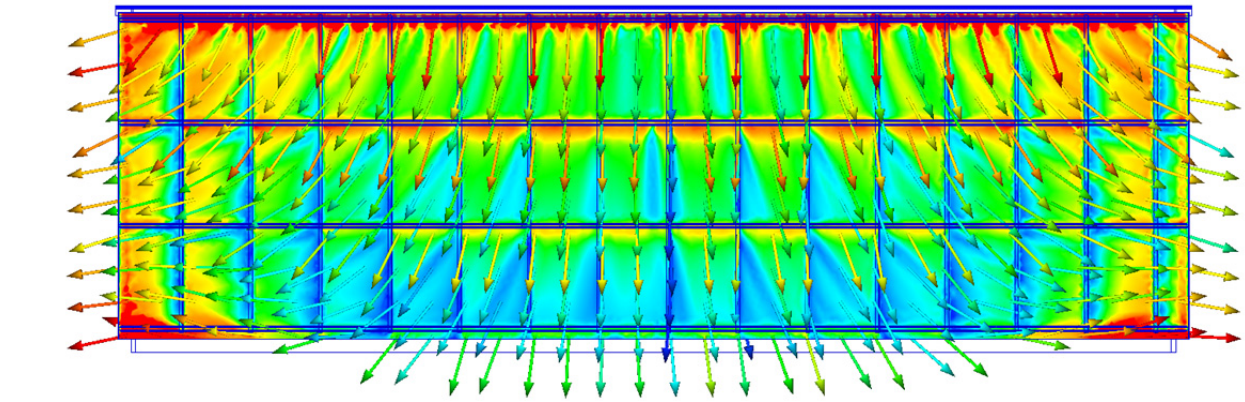

(a)

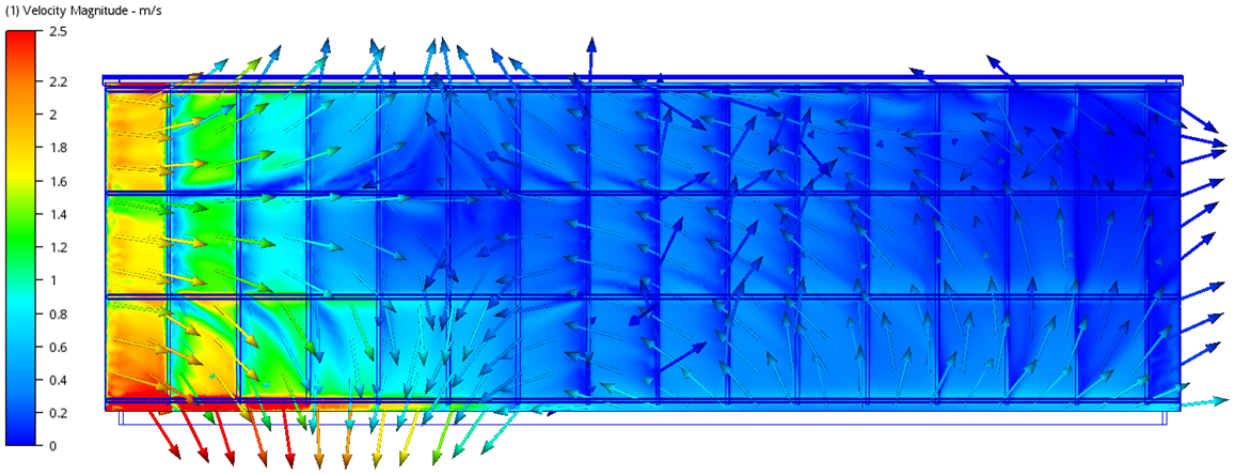

(b)

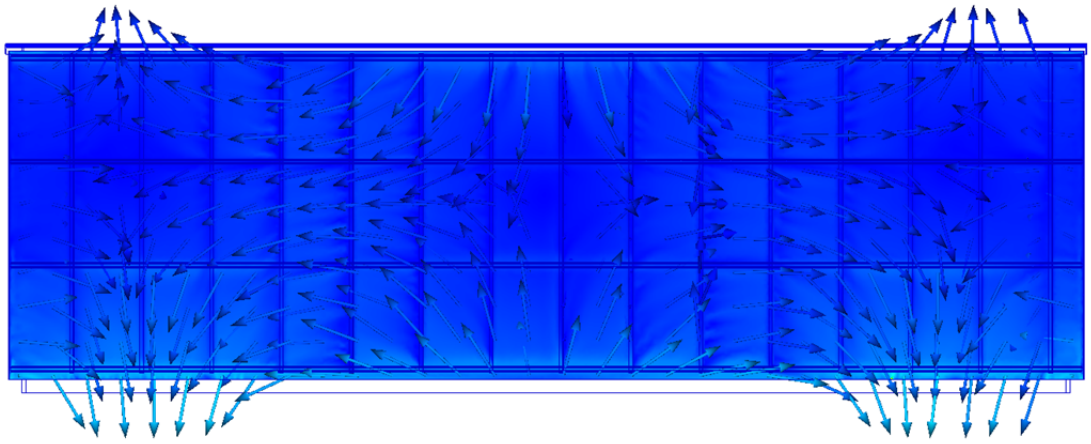

(c)

Fig. 8. Rainscreen air velocity and flow direction at the windward wall (a), side wall (b), and leeward wall (c).

The windward corners of the side walls coincided with the prominent negative pressure regions that occurred on the exterior of the building.

Leeward walls showed even further contrast as air entered from both the upper and lower vents at the center of the wall. The converging flows were then diverted in a near semi-circular pattern back to the upper and lower vents (Fig. 8c). Again, the flow paths were largely determined by the negative pressure on leeward surfaces of the building. Air speed at the referenced section plane ranged between 0.1 to 0.2 m/s.

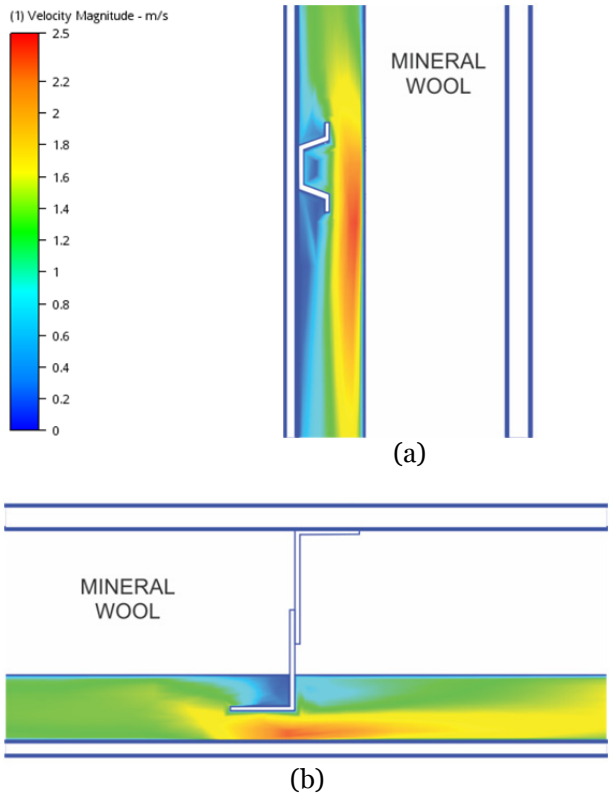

Fig. 9. Section view of air velocity behind a typical hat channel (a) and plan view of air velocity in front of a typical vertical girt (b)

The predicted airflows were characterized by three flow regimes. Highly turbulent flows that ranged from 1.4 m/s to more than 3 m/s were associated exclusively with horizontal hat channels along predominantly vertical flows and at vertical support elements in strong horizontal flows (i.e. corner domains). These dynamic flows were representative of the windward wall as well as the windward corner of the side walls, or approximately 20% of the total ventilated area.

Transitional flows were characterized by turbulent conditions and air speeds that ranged from 0.6 to 1.4 m/s. These flows also occurred at approximately 20% of the total ventilated area. They were found along planar, non-disrupted flow paths of the windward wall and, to a lesser extent, at side walls. Transitional flow regimes also occurred near vent openings of side walls and at much smaller areas of the leeward wall.

The lowest airflow speeds are referenced as semi-stable as they were characterized by both laminar and low turbulence with a velocity range of 0.1 to 0.6 m/s. This flow type was predicted for large areas of the side walls and the entire leeward wall, or approximately 60% of the total ventilated area.

The general airflow paths and semi-stable regimes denoted here align well with much of the prior research involving simpler rainscreen geometries (Salonnvarra et al, 2007; Finch and Straube, 2007, Nore et al., 2010; Falk and Sandin 2013; Straube, et al., 2004; Stovall and Karagiozis, 2004). As illustrated by Figs. 1a and 1b, these traditional rainscreen systems reflect planar flow paths that are often compartmentalized. Venting may or may not be continuous; and the rainscreen depth is generally 20 mm or less.

The higher velocities associated with transitional and highly turbulent flows are more consistent with conditions found in slotted and open rainscreen systems in which velocities of 3 to 6 m/s have been shown in field and simulation studies (Odewole and Edwards, 2011; Mora-Pérez et al., 2014). Still, airflow paths and the general lack of rotational flows are very much consistent with conventional back-ventilated systems. The findings here show that modern rainscreens consisting of complex cladding support framing may actually represent hybrid systems characterized by the flow paths of conventional back-ventilated systems and having the air velocities of slotted or open rainscreen systems. Indeed, the higher velocities reported here for a back-ventilated system are wholly unique to these modern systems having

deeper (i.e. >40 mm) continuous venting and flow-disrupting geometries. Airflows that move in the third dimension, either across or behind the cladding support system, create higher pressure fields that have not been previously reported for back-ventilated systems.

3.3 Heat transfer

Representative flow velocities for the heat transfer wall are shown in Fig. 10. Depicted here is the 1 m/s inlet velocity with the vertical and horizontal flow regimes for the impermeable control. The reference plane represents a section at approximately 12 mm from the mineral wool face. Of particular note is the reduced air velocity predicted for the horizontal inlet condition as compared to the vertical flow. This is in direct contrast to the whole-building simulation, which showed that diagonal and horizontal flows at the windward wall were clearly associated with higher air speeds. This discrepancy is explained by the fact that vertical airflows were diverted against the mineral wool at the hat channels (Fig. 9a). In contrast, air that flowed in a true horizontal manner was diverted outward and around the vertical girt (Fig. 9b). In the whole-building simulation, air was rarely, if ever, flowing in a true horizontal direction. Instead, airflows occurred tangentially against the hat channels. These diverted flows created further turbulence as air moved around the vertical girts. This is further illustrated by Figs. 10a and 10b where vertical airflows behind the hat channel resulted in trailing velocity fields as the air was unobstructed in the primary flow direction (Fig. 10a). Horizontal flow regimes, however, were diverted around the vertical girt, resulting in lower velocities or even stagnant air immediately downstream of the vertical girt (Fig. 10b).

The effects of convective heat loss on heat flux density are shown in Figs. 11a and 11b. The results indicated high correlation (r^2 = 0.95 to 0.99) between mineral wool permeability and increasing heat flux density. As described above, flows in the vertical direction were significantly more causal than horizontal flows, yet the direct relationship between heat flux and permeability is still evident.

For the 1 m/s vertical inlet, heat flux density increased by approximately 4 to 20% as compared to the impermeable control. This range corresponds to mineral wool with estimated densities ranging from 160 kg/m^3 to 30 kg/m^3, respectively. The 2 m/s inlet velocity increased heat transfer by 10 to 42% for the full range of permeability values. Horizontal flows increased heat transfer by approximately 1.5 to 4% at 1 m/s and by 2 to 17% at 2 m/s. Effective R-values corresponding to the increased heat transfers are provided in Table 3.

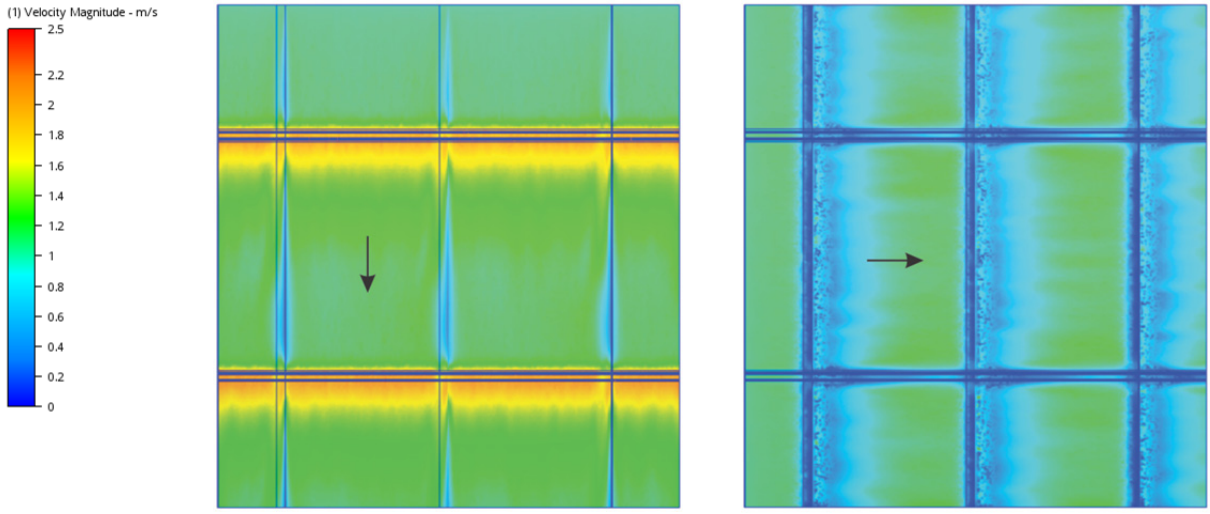

(a) (b)

Fig. 10. Vertical (a) and horizontal (b) airflows at 1 m/s inlet velocity.

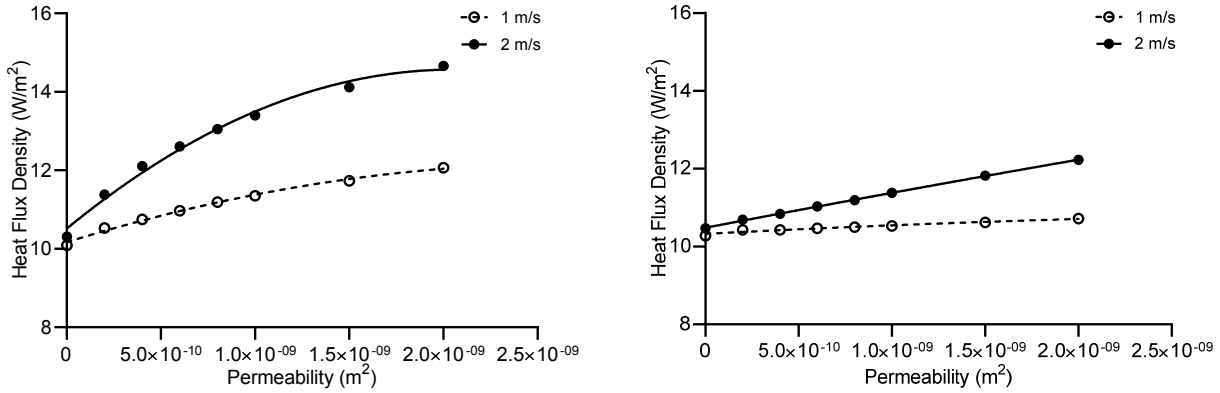

Fig. 11. Heat flux densities in response to vertical (a) and horizontal (b) airflows.

When considering the full permeability range, the corresponding decrease in effective R-value is significant. This reduction is similar to the combined thermal bypasses resulting from wall framing and cladding supports as reported here and by earlier studies (Lawton et al., 2008).

Table 3. Effective R-values of heat transfer walls as reported in imperial units and as RSI (SI)

Permeability (m^2)	Vertical Flow		Horizontal Flow	
	1 m/s	2 m/s	1 m/s	2 m/s
0 (solid)	14.6 (2.57)	14.3 (2.52)	14.3 (2.52)	14.1 (2.48)
2.0 x 10^{-10}	14 (2.47)	13.0 (2.29)	14.1 (2.48)	13.8 (2.43)
4.0 x 10^{-10}	13.7 (2.42)	12.2 (2.15)	14.1 (2.48)	13.6 (2.39)
6.0 x 10^{-10}	13.4 (2.36)	11.7 (2.06)	14.1 (2.48)	13.4 (2.36)
8.0 x 10^{-10}	13.2 (2.32)	11.3 (1.99)	14.1 (2.48)	13.2 (2.32)
1.0 x 10^{-9}	13.0 (2.29)	11.0 (1.94)	14.0 (2.47)	13.0 (2.29)
1.5 x 10^{-9}	12.6 (2.22)	10.5 (1.85)	13.9 (2.45)	12.5 (2.20)
2.0 x 10^{-9}	12.2 (2.15)	10.1 (1.78)	13.8 (2.43)	12.1 (2.13)

The increase in convective heat loss is attributed to wind-washing of mineral wool surfaces as well air penetration into the open pore volume. The combined effects of air permeability and heat loss are demonstrated by Figs. 12a and 12b, which show airflow velocities and corresponding temperature profile near a horizontal hat channel.

Airflows within the open pore volume were multi-directional and complex as reflected by diverging airflows, converging airflows, and rotational eddies. Prevailing airflow directions were determined by the angle of entry, airflow velocity, and pressure gradients within the rainscreen air volume. Air within the mineral wool generally flowed in parallel to the primary rainscreen flow. In contrast, movement perpendicular to rainscreen flow dominated where rainscreen airflows were disrupted by hat channels or vertical girts and then deflected toward the mineral wool.

Flow velocities within the mineral wool varied based on permeability and distance from the rainscreen air. For example, Fig. 13 illustrates flow velocities through the depth of the mineral wool slab where simulations involved a vertical inlet velocity of 1 m/s and a permeability of 1.0 x 10^{-9}. For this particular section plane and simulation conditions, velocities at the typical vertical field ranged from approximately 0.0001 to 0.002 m/s at a static pressure of 24 Pa. Where diverted inward near the horizontal hat channel, air speeds within

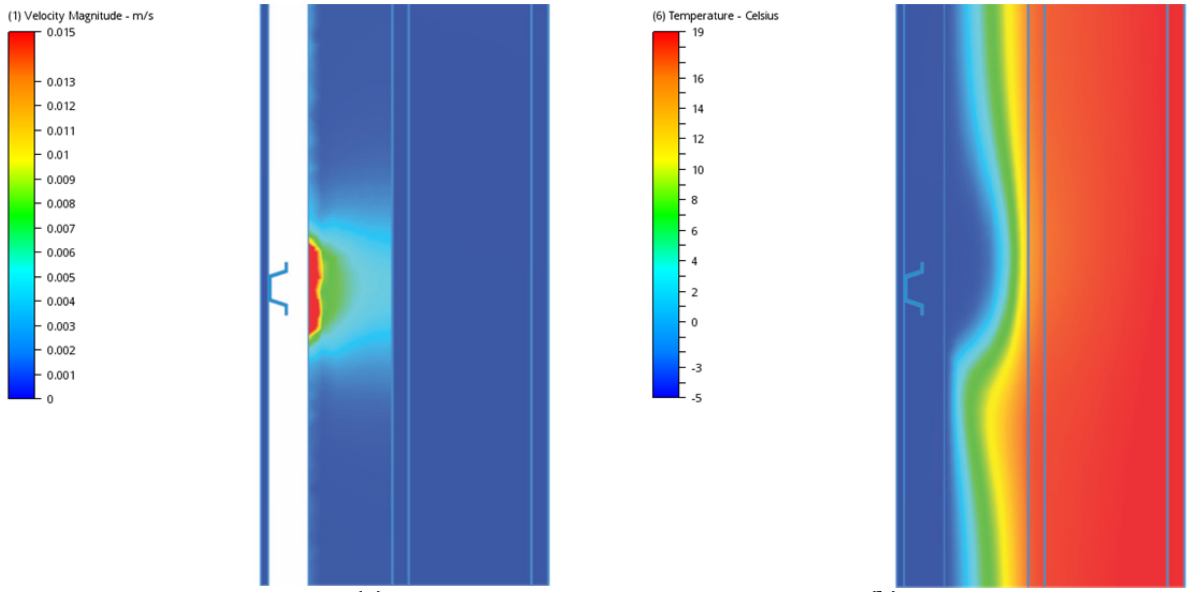

Fig. 12. Section views of air velocities through mineral wool (a) and corresponding wall temperature profile (b).

the mineral wool increased by more than a factor ten, ranging from approximately 0.001 to 0.05 m/s at a static pressure of 40 Pa. Higher velocities were predicted in proximity to the rainscreen air cavity. In this specific example, velocities decreased sharply as air moved into the mineral wool to a depth of approximately 15 mm. Flows then remained relatively unchanged until approaching the backup wall. The flows reported here are very similar to the flow-through velocities measured by Schmidt and Kornadt (2012) for similar pressures and mineral wool density.

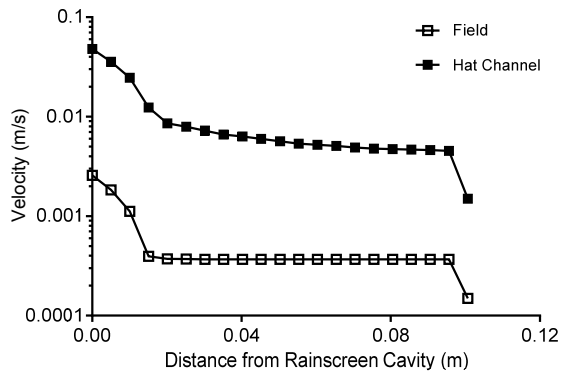

Fig. 13. Air velocity through a mineral wool profile.

Discussion regarding the permeability of mineral wool should take into account that slabs are anisotropic in that individual fiber layers are oriented parallel to the slab's broad surface. This orientation results in significantly higher air permeability when airflows occur against the lateral plane. Correlations of air resistivity with rock wool density for lateral and longitudinal airflows are provided by Hopkins (2007). These data show that air permeability for airflow against the lateral plane is approximately 50% higher than permeability in longitudinal airflow. The longitudinal data reported by Hopkins (2007) also show good agreement with resistivity values typically provided by mineral wool manufacturers. The referenced longitudinal and lateral airflows as referenced by the mineral wool industry are illustrated by Fig. 14.

Air resistivity data for fibrous insulation products are typically derived from methods intended for acoustic testing in accordance with ISO 9053/EN 29053. This standard employs a pressure differential of 0.2 Pa, which corresponds to a particle velocity of $0.5 \cdot 10^{-3}$ m/s at a sound pressure of 80 dB (del Ray et al, 2013). The applicability of such low pressure differences has been questioned by Schmidt and Kornadt (2012) who found that

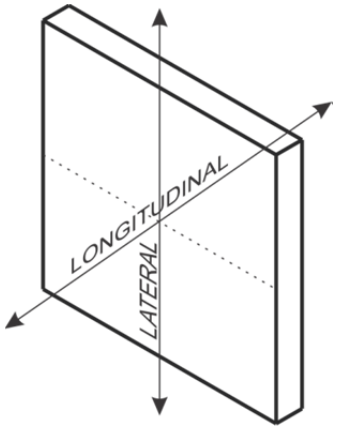

Fig. 14. Referenced airflow planes.

longitudinal permeability of rock wool slabs was more than 30% higher when measured at realistic rainscreen pressure differences of 5 to 10 Pa as compared to earlier findings that utilized the 0.2 Pa standard for acoustic testing.

The above concerns demonstrate that many factors, other than air speed determine the movement of air through the open pore volume of mineral wool. When combined with the findings discussed herein, they point to three important considerations.

First, the permeability values reported by mineral wool manufacturers should be reviewed critically. If the data reflect acoustic methodologies such as those outlined by ISO 9053/EN 29053, then adjustment should be made for increased air permeance to reflect actual in-service conditions.

Second, although this study applied a constant permeability in all directions, care was still taken to avoid inlet flows directly against the lateral surface. Such provisions for preventing higher flow rates through lateral surfaces are not necessarily practiced by the construction industry. Therefore, when combined with the above considerations for pressure-dependence, the industry's reliance on manufacturer's reported data may actually underestimate permeability by approximately 90%. This is equivalent to the change in permeability corresponding to a density of 70 kg/m^3 to a more permeable product with a density of 50 kg/m^3.

Third, the effects of convective heat loss through permeable mineral wool were pronounced and potentially relevant to moisture performance. For example, localized heat loss reduced surface temperatures at other wall components as shown by Fig. 15. In these particular examples,

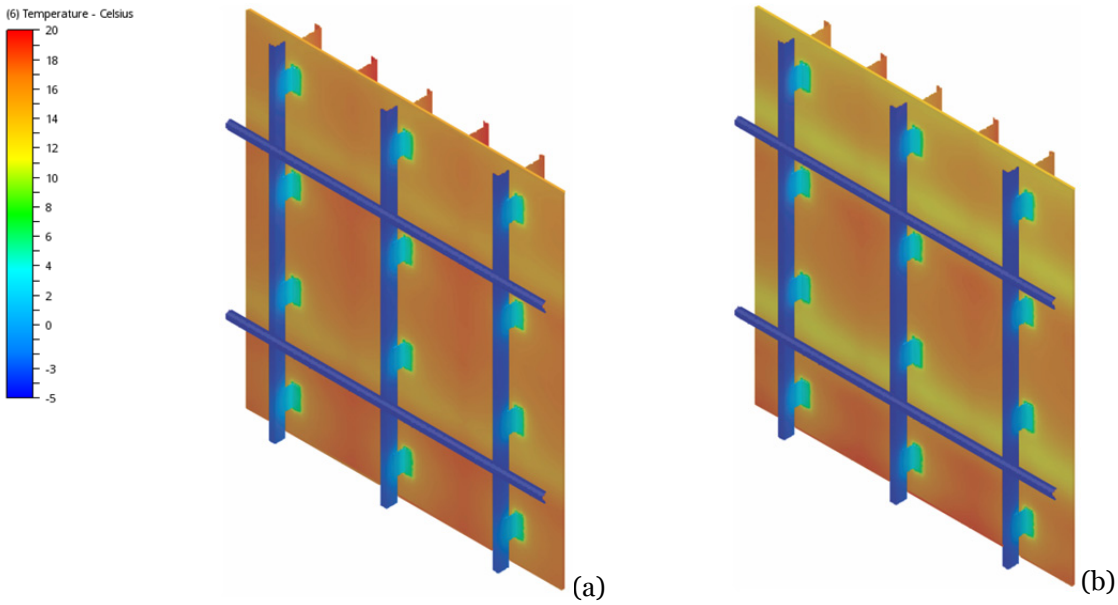

Fig. 15. Thermal fields at exterior surfaces of wall sheathing.
Vertical inlet velocities were 1 m/s (a) and 2 m/s (b)

wall temperature near the horizontal hat channels was reduced by 2 to 5°C. Considering the total affected area, such shifts warrant greater consideration for the indirect effects on moisture transport. More severe thermal shifts such as those resulting from increased wind speeds, air gaps, or lower exterior temperature may approach the dew point.

The convective effects predicted by these simulations were more pronounced than those shown by earlier studies for comparable mineral wool slabs (Stankevičius et al., 2013; Stratten and Trainor, 2013). What is not reflected by this prior research is the effect of higher air speeds and, multi-directional airflows created by modern rainscreen geometries. These systems to which mineral wool are now applied are very different and they demand more critical evaluation when considering true energy performance. Furthermore, the ramifications of convective heat loss underscore the need for adjustments in effective R-values when using un-faced mineral wool slabs. The effective R-values reported in Table 3 may serve as a guide in this approach. It should be noted, however, that even greater adjustments may be necessary when considering open rainscreen systems and more intense, complex flows. For example, air speeds predicted by the simplified flow regimes did not necessarily demonstrate the synergistic effects shown by the whole-building simulation.

3.4. The effects of air gaps

It is recognized that gaps between mineral wool slabs and their adjacent enclosure components are unavoidable (Stankevičius et al., 2013). The effects of air gapping are therefore important, especially in systems that rely exclusively on exterior insulation. This gap study represented a two-phased approach. The effects of forced convection were first assessed with vertical and horizontal gaps that were 3.2 mm wide. The second phase combined these gaps with a thin (0.8 mm) air film behind the mineral wool slab. Both simulations involved a single permeability of 1.0 x 10^{-9} as representative of an insulation density of 50 kg/m^3.

Table 4 summarizes the effects of horizontal and vertical gaps. These results show that edge gaps increased heat loss by approximately 3 to 6% as compared to the same slabs without gaps. Introduction of the thin air film increased heat transfer even more. At 1 m/s, the combined gaps increased heat loss by 19 to 21% as compared to the non-gapped slabs. The higher air flow of 2 m/s showed similar increase of 24 to 25%. When compared to the non-gapped impermeable condition, the combined gaps increased heat transfer by approximately 62%, which corresponds to an effective R-value of 8.8 (Btu/hr/ft^2) or an RSI of 1.6 (Km^2/W).

The increase in convective heat loss is attributed to bulk air entry into the edge gaps. This is particularly prominent where edge gapping interfaces with the inlet or where vertical girts and hat channels divert air against the mineral wool. When just edge gapping was present, wind-washing of the wall sheathing was limited due to the small interfacing surface area. Air that entered the gap was forced into the open pore volume; or it was diverted outward in response to pressure gradients established by the rainscreen cavity flow.

Table 4. Heat flux densities for gap conditions.

	Heat Flux Density W/m^2 (Btu/hr/ft^2)		
	No Gaps	Edge Gaps	Interstitial Gap
1 m/s: vertical airflow	11.4 (3.60)	11.9 (3.78)	13.5 (4.27)
1 m/s: horizontal airflow	10.5 (3.34)	11.1 (3.51)	12.7 (4.04)
2 m/s: vertical airflow	13.4 (4.25)	13.9 (4.40)	16.7 (5.31)
2 m/s: horizontal airflow	11.4 (3.61)	11.8 (3.75)	14.1 (4.48)

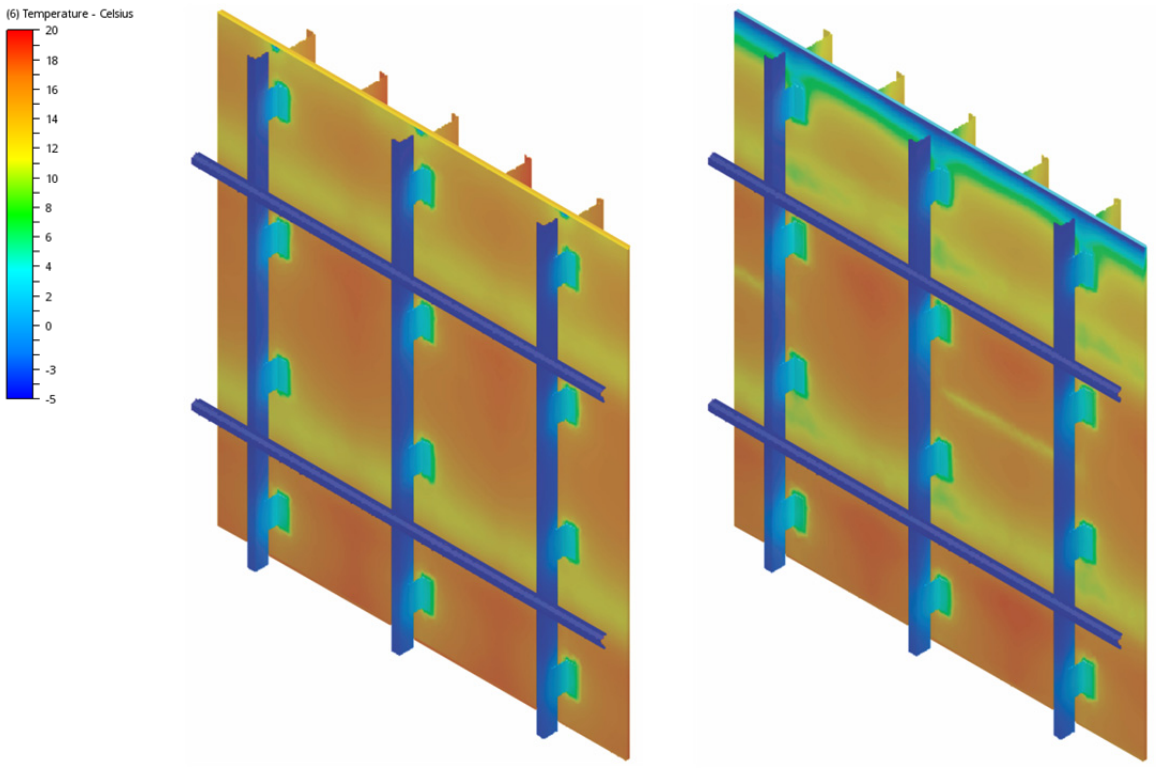

Fig. 16. Temperature at exterior surfaces of wall sheathing in response to edge gaps (a) and combined edge and interstitial gaps (b).

Introduction of the thin airspace behind the insulation provided the pressure differential necessary for air to move more freely through the gap network and within the open pore volume of the mineral wool. Simulations predicted that movement through the edge gaps occurred bi-directionally (i.e. inward and outward). Although direct cycling between the interstitial space and the colder rainscreen air volume did occur, the resulting effects on heat loss were tempered by the more pervasive recycling of air between the mineral wool and interstitial gap.

Further resolution of these complex dynamics can be made by analyzing thermal fields at exterior surfaces of the wall sheathing (Fig. 16). Both assemblies shown in Fig. 16 represent the vertical inlet condition at 2 m/s with a representative permeability of 1.0 x 10^{-9}. With edge gaps alone (Fig. 16a), the effects were relatively unchanged from the non-gapped condition shown earlier in Fig 15b. Of interest, however, was localized cooling of the sheathing where the top inlet interfaced with the vertical gaps. This effect was significantly more pronounced with the combined gap condition where inlet cooling extended the full width of the assembly (Fig. 16b). In both cases, the need to protect slab edges is reinforced, especially for inlet conditions. Figure 16b also shows that the interstitial gap facilitated localized air exchange at edge gaps, as evidenced by the two horizontal gaps at mid-wall height. The vertical gaps figured even more prominently by exacerbating localized heat loss when air is forced into the mineral wool behind the horizontal hat channels (Fig. 16b).

What is evident from the above assessment is that the introduction of edge gaps with the thin interstitial gap did not result in widespread washing of the sheathing face. On the contrary, the effects were localized but significant nonetheless as the predicted sheathing temperatures at affected areas were below expected dew points. These effects will likely increase with increased gap size, increased wind speed, and reduced exterior temperatures.

Modeling the insulation as an impermeable solid resulted in even greater heat loss. This is attributed to the fact that the same pressure differential acts on a more discrete area (i.e. the gap itself) as opposed to the greater permeable matrix.

These findings emphasize the need for avoiding air gaps between slabs and other rainscreen components. The authors contend that simply butting the slab joints together is insufficient due to varied workmanship and prevailing perceptions that small gaps are inconsequential. The gap dimensions used in this study were reflective of common construction practices. As demonstrated by this study, these gaps do not need to be continuous to have notable effect. Furthermore, interstitial gapping behind the mineral wool is inevitable without adhering the slab to the backup wall in a continuous manner. Pinning may be ineffective due to planar distortions, which often results in gaps that are even more pronounced than the 0.8 mm space employed by this study.

The inherent nature of air-permeable exterior insulation requires special considerations for convective heat loss. Such concerns have influenced European practices towards faced-materials or separate air barrier layers over the otherwise exposed mineral wool face. This idealized approach further entails fully-adhered slabs with robust joint treatments.

4. CONCLUSIONS

Comprehensive CFD simulations of convective heat transfer were presented for a ventilated rainscreen system. This empirical evidence validates longstanding concerns regarding wind-induced convection and its effects on heat loss through exterior mineral wool. Our main findings were:

(1) Rainscreen air velocities of 0.1 to 3 m/s were predicted for an exterior wind speed of 6.7 m/s (15 mph). These air speeds are higher than those reported for classical back-ventilated systems that have simpler geometries and more planar flow paths. The higher velocities shown here were associated with specific vertical and horizontal elements of the cladding support system. Airflows that move in the third dimension, either across or behind the cladding support system, create higher pressure fields that have not been previously reported for back-ventilated systems. This suggests that such rainscreens exhibit the flow characteristics of conventional back-ventilated systems while having localized velocities more similar to slotted or open-jointed rainscreens.

(2) Heat transfer studies demonstrated that forced convection increased heat flux density by approximately 4 to 42%. This range corresponds to mineral wool with estimated densities ranging from 160 kg/m^3 to 30 kg/m^3, respectively. Effective R-values were reduced by approximately 30%. This reduction is similar to the combined thermal bypass resulting from wall framing and cladding support system.

(3) Airflows within the mineral wool were multi-directional and complex. Prevailing airflow directions were determined by the angle of entry, airflow velocity, and pressure gradients within the rainscreen air volume. Air within the open pore volume generally flowed in parallel to the primary rainscreen flow. In contrast, movement perpendicular to rainscreen flow dominated where rainscreen airflows were disrupted by hat channels or vertical girts. Rainscreen geometries therefore played a very important role in determining flow paths and air speed through the mineral wool.

(4) Combining edge gaps with interstitial gaps behind the mineral wool slabs increased heat loss by 19 to 25% as compared to the non-gapped condition. In comparison, convective heat loss increased by approximately 62% as compared to non-gapped, impermeable insulation.

(5) The effects of convective heat loss through permeable mineral wool were pronounced and potentially relevant to moisture performance. Conditions such as gaps,

increased wind speed, lower exterior temperature, or higher indoor relative humidity increase the potential for moisture problems.

(6) These findings underscore the need for enhanced design and construction practices. Alternatively, adjustments in effective R-values should be made when using un-faced mineral wool slabs.

5. REFERENCES

American Society of Civil Engineers. 2010. Minimum design loads for buildings and other structures. Reston, VA: American Society of Civil Engineers

American Society of Heating, Refrigerating, and Air-Conditioning Engineers. 2009. ASHRAE handbook: Fundamentals. Atlanta. GA: American Society of Heating, Refrigerating, and Air-Conditioning Engineers.

Autodesk Simulation CFD Help Desk. 2016. https://knowledge.autodesk.com/support/cfd/downloads/caas/downloads/content/cfd-2016-download-and-install-help-documentation.html. Updated:12-28-2015

Casey M, Wintergerste T. 2000. ERCOFTAC Best Practice Guidelines, Special Interest Group on Quality and Trust in Industrial CFD. Version 1.0 . Published by ERCOFTAC, 2000.

del Ray R, Alba J, Arenas JP, Ramis J. 2013. Evaluation of two alternative procedures for measuring airflow resistance of sound absorbing materials. Archives of Acoustics. Vol. 38, No. 4: 547-554.

Endriukaitytė A, Parasonis J, Bliūdžius R. 2009 . Building envelope insulation rock wool. science book / Gediminas Technical University. Vilnius: Technika, 2009. 164 p . ISBN 978-9-9552-8540-3.

Falk, J, Sandin K. 2013. Ventilated rainscreen cladding : Measurements of cavity air velocities, estimation of air change rates and evaluation of driving forces. Building and Environment: 59, 164–176.

Finch G, Straube J. 2007. Ventilated wall claddings: review, field performance and hygrothermal modeling. Thermal Performance of the Exterior Envelopes of Whole Buildings X. Clearwater, FL. ASHRAE Pulications.

Hens H, Janssens A, Depraetere W. 2001. Hygrothermal performance of masonry cavity walls with very low U-factor: a test house evaluation. Proceedings of ASHRAE THERM VIII, Clearwater, FL.

Hopkins C. 2007. Sound Insulation. Published by Elsevier Ltd. ISBN: 978-0-7506-6526-1. 648 p:79-82.

Huttunen P, Vinha J. 2013. Effect of Natural Convection on the Thermal Transmittance of Exterior Walls with Air-Permeable Insulation. Thermal performance of the exterior envelopes of whole buildings XII international conference. ASHRAE.

ISO 9053/EM 29053. 1993. Acoustics. Materials for acoustical applications. Determination of airflow resistance. ISBN 0-580-21966-6.

Kosiński, P. 2014. An impact of air infiltration on heat transfer through lightweight building partitions filled with loose mineral wool. Ph.D. Thesis. The University of Warmia and Mazury in Olsztyn.

Kosiński P. 2015. Thermal bridge effect of air gaps in wall construction, Technical Sciences. 18(3) 159-169.

Lawton M, Roppel P, Fookes D, Teasdale A, Schoonhoven D. 2008. Real R-value of exterior insulated wall assemblies. BEST 1 Conference Proceedings. Building Enclosure Science & Technology. Minneapolis, Minnesota, June 10-12, 2008.

Lecompte J. 1990. The influence of natural convection on the thermal quality of insulated cavity construction: results of experimental research and computer simulation. Building Research and Practice. The Journal of CIB. 18:349-354.

Mora-Pérez M, López-Patiño G, López-Jiménez AP. 2014. Quantification of Ventilated Façade Effect Due to Convection in Buildings-Buoyancy and Wind Driven Effect. Researches and Applications in Mechanical Engineering. Volume 3.

Odewole A, Edwards R. 2011. The characteristics of the velocity field in a slot-ventilated wall cavity. ARPN Journal of Engineering and Applied Sciences Vol 6 (10): 47–55.

Nore K, Blocken B, Thue JV. 2010. On CFD simulation of wind-induced airflow in narrow ventilated faced cavities: coupled and decoupled simulation and modeling limitations. Building and Environment. 45:1834-1846.

Paroc. 2016. Design guidelines for ventilated facades. http://www.paroc.com/solutions-and-products/design/ventilated-facades?sc_lang=en.

Salonvaara MH, Karagiozis AN, Pazera M, Miller W. 2007. Air Cavities Behind Claddings— What Have We Learned?. Thermal Performance of the Exterior Envelopes of Whole Buildings Tenth International Conference. Clearwater Beach, FL, December 2–7 2007.

Schmidt J, Kornadt O. 2012. Convection through light weight timber construction with mineral wool. International Scholarly and Scientific Research & Innovation. 6:425-432.

Straaten BR Van, Trainor T. 2013. Effects of Wind Washing on Roxul Mineral Wool Sheathing in Low-rise Residential Buildings. Short Reports, Building Science Labs: 1–11.

Stankevičius V, Paukštys V, Bliūdžius R, Šadauskienė J, Turskis Z, Samajauskas R. 2013. Convection in mineral wool used as insulation for buildings. J. Civ. Eng. Manag. 19:296-304.

Stovall T, Karagiozis A. 2004. CFD Analysis of a ventilated brick cavity. Annex 41 Report A41-TI-US-04-2.

Straube J, VanStraaten R, Burnett E, Schumacher C. 2004. Review of literature and theory. Report #1-ASHRAE 1091. University of Waterloo. Canada

Svoboda Z. 1999. The Analysis of the Convective-Conductive Heat Transfer in the Building Constructions. Proceedings of the 6th Int. IBPSA Conference Building Simulation, Kyoto. vol. 1: 329—335.

Van Straaten R, Trevor T. 2014. Effects of wind washing on Roxul mineral wool sheathing in low-rise residential buildings. Building Science Laboratories.